RSC Advances

PAPER

View Article Online
View Journal | View Issue

Cite this: *RSC Adv.*, 2025, **15**, 13086

Single step site-selective reaction to construct a $Ag_2Au_2 \leftarrow Ag_4$ supramolecular assembly from hybrid N-heterocyclic carbene (NHC): synthesis, structures and optoelectronic properties†

Pooja Das,[a] Soumi Halder,[bc] Partha Pratim Ray,[b] Narayan Ch. Jana,[d] Priyanka Sahu,[a] Anvarhusein A. Isab,[e] Rambabu Dandela,[f] Ramalingam Natarajan[g] and Joydev Dinda*[a]

Two supramolecular complex assemblies, $[Ag_4(\mathbf{1})_2][PF_6]_4 \cdot 4MeCN$ **2** and Ag(I)–Au(I) mixed metal complex $[Ag_2Au_2(\mathbf{1})_2][PF_6]_4 \cdot 4MeCN$ **3**, have been prepared from 3-(pyridylmethyl)imidazo[1,5-*a*]pyridin-4-ylium hexafluorophosphate (**1** HPF_6), which is the precursor of N-heterocyclic carbene (NHC). These complexes were subsequently analyzed using various spectroscopic techniques to confirm their structural and chemical properties. Transmetallation of Au(I) onto the Ag_4 macrocycle results in the formation of an Ag_2Au_2 macrocyclic assembly. Au(I) selectively binds with the soft donor $C_{carbene}$, whereas Ag(I) binds with comparatively hard donor N_{py} (py = pyridine). The geometries of **2** and **3** were established by single-crystal X-ray diffraction studies. Both molecules form a 2D network through M–M and several non-covalent interactions. Electrical conductivity measurements revealed that Ag(I) complex **2** is better conductor than Au(I) complex **3**. Optoelectronic studies revealed the utility of complexes **2** and **3** as photovoltaic devices. Furthermore, MS-junction potential measurements show that they are suitable for semiconductor devices, with complex **2** being more efficient than complex **3**. Finally, in this study, we aimed to explore the scope of (i) the development of heterobimetallic supramolecular organometallic complexes (SOC), (ii) the charge transport behaviour of SOCs, and (iii) the modification of intrinsically conductive SOCs-based electronics.

Received 29th January 2025
Accepted 8th April 2025

DOI: 10.1039/d5ra00684h

rsc.li/rsc-advances

Introduction

In the past few decades, extensive research on supramolecular coordination complexes (SCCs)[1] has drawn significant attention within the field of coordination chemistry. The diverse areas of application have created interest in these compounds. Until now, the scope of SCCs has been explored in drug delivery,[2] molecular recognition,[3] catalysis,[4] and the stabilization of highly reactive species,[5] among other applications. The most accepted method used for the construction of SCCs is coordination-driven self-assembly.[6] From the ligand point of view, multitopic ligands are capitalized upon to construct metallosupramolecular assemblies; the ligands mostly carry Werner-type O-, N- and P-donor sites. Beyond the common O-, N- and P-donor atoms, researchers have also explored C-donor ligands. This led to the development of poly-N-heterocyclic carbene (NHC) ligands,[7] which serve as strong C-donor ligands for constructing supramolecular organometallic complexes (SOCs). These NHC-based SOCs are a subclass of metallosupramolecular assemblies, where metal–carbon (M–C) bonds play a crucial role in stabilizing diverse architectures.[7–9] The rapidly growing class of organometallic supramolecular assemblies, referred to as supramolecular organometallic complexes (SOCs), was initially reported by Pothig and Casini.[10] Further studies on the biological importance of SOCs were also reported,[10] where linker-metal connections are established by M–C bonds.

Nowadays, the number of supramolecular organometallic complexes (SOCs) featuring M–C bonds has grown steadily. In particular, NHC-based SOCs, which incorporate poly-NHC

[a]*Department of Chemistry, Utkal University, VaniVihar, Bhubaneswar-751004, Odisha, India. E-mail: joydevdinda@gmail.com; joydevdinda@utkaluniversity.ac.in*
[b]*Department of Physics, Jadavpur University, Kolkata-700032, WB, India*
[c]*Department of Physics, Vidyanagar College, South 24 Parganas, West Bengal 743503, India*
[d]*School of Chemical Sciences, National Institute of Science Education and Research, HBNI, Bhubaneswar, Odisha 752050, India*
[e]*Department of Chemistry, King Fahd University of Petroleum and Minerals, Dhahran 31261, Saudi Arabia*
[f]*Department of Chemistry, Indian Institute of Chemical Technology, Bhubaneswar-751004, Odisha, India*
[g]*Department of Chemistry, CSIR-Indian Institute of Chemical Biology, Kolkata-700032, West Bengal, India*

† Electronic supplementary information (ESI) available. CCDC 2271882 and 2271883. For ESI and crystallographic data in CIF or other electronic format see DOI: https://doi.org/10.1039/d5ra00684h

ligands as key structural elements, have been extensively reported, especially for group 11 metals such as silver. Coinage metals in the +1 oxidation state form linear $C_{carbene}$–M–$C_{carbene}$ linkages that essentially construct the fundamental building blocks.[8c,d] Importantly, the labile Ag–$C_{carbene}$ bond facilitates rearrangement to form the thermodynamically most stable assembly (see d/b ratio is 7.8–12.68, d = donation, b = back donation of electron); as a result, diverse architectures such as rectangles, triangles,[11] cylinders[12] and barrels[12f] have been obtained. Hahn's group was the first one to exploit square- and rectangular-shaped supramolecular organometallic assemblies incorporating transition metals such as gold,[13] iridium,[14] platinum,[15] palladium,[16] and nickel.[17] Although there has been significant development in supramolecular organometallic assemblies in recent years, their applications remain largely focused on host–guest chemistry. Beyond this, Mukherjee's group has developed Ag(I)–NHC-based supramolecular assemblies for picric acid sensing,[18a] artificial light harvesting,[18b] and the detection of the broad-spectrum pesticide 2,6-dichloronitroaniline (DCN).[18c] Altmann and Pöthig have reported the encapsulation of organic substrates into Ag_8 and Au_8 pillarplexes.[19] Rit's group has also reported trinuclear and tetranuclear supramolecular organometallic assemblies of coinage metals developed by NHC ligands.[20] Peris has developed Pt(II) SOCs that function as receptors for electron-deficient organic molecules such as 1,4,5,8-naphthalenetetracarboxylic dianhydride (NTCDA), 1,2,4,5-tetracyanobenzene (TCNB), and 2,4,7-trinitro-9-fluorenone (TNFLU).[21] Our group also reported a helical Hg(II) SOC.[22]

The architecture of metallosupramolecular complexes incorporating poly-NHC ligands and transition metals is a promising strategy.[8a,14] Very recently, we reported an atom-selective reaction on an Ag_3 cluster, which led to an Ag_2Au mixed-metal cluster stabilized by a pincer NCN-carbene.[23] Herein, we have introduced a multitopic hybrid-NHC ligand bearing C- and N-donor centers, assuming that M–$C_{carbene}$ will form a linear bond and $N_{pyridine}$ will extend the coordination, resulting in a metallosupramolecular assembly. We have constructed an Ag_4 cage-like structure tailored by the C, N-donor NHC ligand; while transmetallation leads to an Ag_2Au_2 heterometallic supramolecular complex, where Au(I) selectively binds with $C_{carbene}$ and Ag(I) binds with $N_{pyridine}$. Thus, inspired by recent findings, we have successfully synthesized and characterized the Ag_4 coordination assembly and explored its optoelectronic properties, particularly the variation in electrical conductivity in dark and light, given silver's long-standing history in photoelectric properties.[24]

Incorporation of a second transition metal into the supramolecular framework is also an important area of research, as the resulting coordination motifs provide opportunities to tailor the properties and functionalities of these materials to meet specific application requirements.[24] Moreover, the incoming second metal selectively binds with the multitopic ligand. This site-specific bonding has been observed with several metals and facilitates the development of heterobimetallic and heterometallic systems.[25] The construction of heterometallic systems is a highly promising field of research due to their elegant architectures and interesting properties. They span wide-ranging fields such as bioinorganic chemistry, materials science, photophysics artificial photosynthesis, redox- and photoactive polymers, nanoscience, catalysis, sensors, and optoelectronic chemistry, among others.[26] In recent years, scientists have increasingly focused on developing smart functional materials for constructing electronic and optoelectronic devices, with the goal of achieving robust electrical conductivity. This property in a metal complex can be achieved either through a continuous chain of coordination bonds between metal centers and ligands, or *via* non-covalent interactions. Among these, π–π stacking interactions between organic moieties within the molecular framework play a crucial role in enhancing electrical conductivity.[27] Although numerous organic ligands embedded with various transition metals have been synthesized in the search for better performing optoelectronic materials, NHC ligand framework with silver or gold metals remain largely unexplored.

Based on abovementioned findings, we present a novel NHC-based SOC constructed using a site-selective metallation approach. The ligand 3-(pyridylmethyl)imidazo[1,5-*a*]pyridin-4-ylium hexafluorophosphate, a multitopic NHC precursor, facilitates the formation of the Ag_4 supramolecular complex **2**. Furthermore, successful transmetallation of complex **2** with the gold precursor Au(SMe_2)Cl resulted in Ag_2Au_2 supramolecular organometallic complex **3** (Chart 1). Due to the extended conjugation and several interactions within the molecular framework of complexes **2** and **3**, their electrical conductivity and potential application in electronic devices were also studied.

Results and discussion

3-Picolyl wingtip imidazolium based-NHC carbene precursor (**1** HPF_6) was prepared (Scheme 1) following a reported procedure.[28] The formylative cyclization was carried out on the Schiff base of pyridine-2-carboxaldehyde and 3-picolylamine. The formation of the carbene precursor was confirmed by the appearance of the imidazolium NCHN- proton signal at 9.54 ppm in the ^{1}H NMR spectrum and the procarbenic signal at 147.7 ppm in the ^{13}C NMR spectrum. The reaction of **1** HPF_6

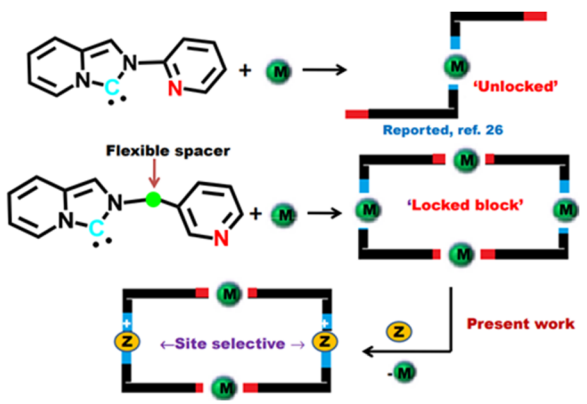

Chart 1 Schematic of the spacer role and of the site selectivity nature of Au(I).

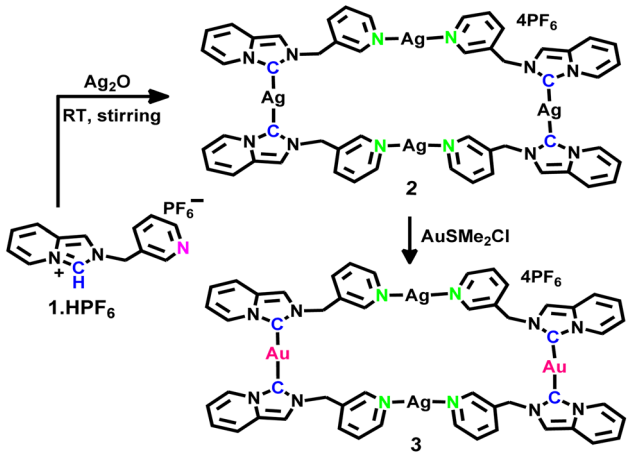

Scheme 1 Site selective metallation of **1** HPF_6 with Ag(I) and Au(I). The letters surrounding **1** refer to the NMR assignments; see the Experimental section.

with Ag_2O afforded the tetranuclear complex **2**, which was followed by transmetallation with gold(I) using $Au(SMe_2)Cl$, yielding the tetranuclear complex **3**. Reaction of **2** with $Au(SMe_2)Cl$ in 1 : 2 and 1 : 4 ratios yielded the same product **3**; this establishes a site-selective reaction.

Experimental section

The disappearance of the imidazolium proton signal ($\delta = 9.54$ ppm) (Fig. S1†) in the ^{1}H NMR spectrum and the downfield shift of the ^{13}C NMR signal at 165.02 ppm (the signal of the free proligand appears at 147.71 ppm) (Fig. S2†) confirm the formation of complex **2** (as shown in Fig. S3 and S4†). Similarly, the disappearance of the imidazolium proton and a downfield shift of the carbenic carbon at 173.02 ppm confirm the formation of complex **3** (as shown in Fig. S5 and S6†). The formation of a self-assembled single product was confirmed by ^{1}H diffusion-ordered NMR spectroscopy (DOSY NMR) (as shown in Fig. S7 and S8†). HR-MS analysis of the proligand **1** HPF_6, showing a peak at 210.1030 *m/z*, supports the proposed formulation of proligand (Fig. S9†). ESI-MS analysis provided the exact stoichiometry of complexes **2** and **3**. For complex **2**, the charged fragment $[Ag_3L_2][PF_6]_3$ was identified by a prominent peak at $m/z = 1175.1194$ (Fig. S10†). In the case of complex **3**, the fragments $[AuL_2]$ and $[AuAgL_2][PF_6]$ were indicated by significant peaks at $m/z = 615.1282$ and 867.0345, respectively, (Fig. S11†). Complexes **2** and **3** show absorption maxima (λ_{max}) at 271 and 277 nm, respectively (Fig. 2). The FTIR spectra (Fig. S12†) show a notable decrease in the imidazole ring streching bands (C=N and C–N), observed at ~1053 and 1444 cm^{-1} for complex **2** and ~1038 and 1438 cm^{-1} for complex **3**, compared to those in the corresponding NHC proligands (~1060 and 1450 cm^{-1}). This shift strongly supports the formation of the desired carbene complexes.

We have further performed single-crystal X-ray diffraction measurements to determine the molecular identity of complexes **2** and **3** (Fig. 1a and c). Single-crystal X-ray diffraction analysis revealed that crystals of complexes **2** and **3** belong to the triclinic crystal system in the space group *P*1 (as shown in Table S1†). In the asymmetric unit of complex **2**, half of a dimer

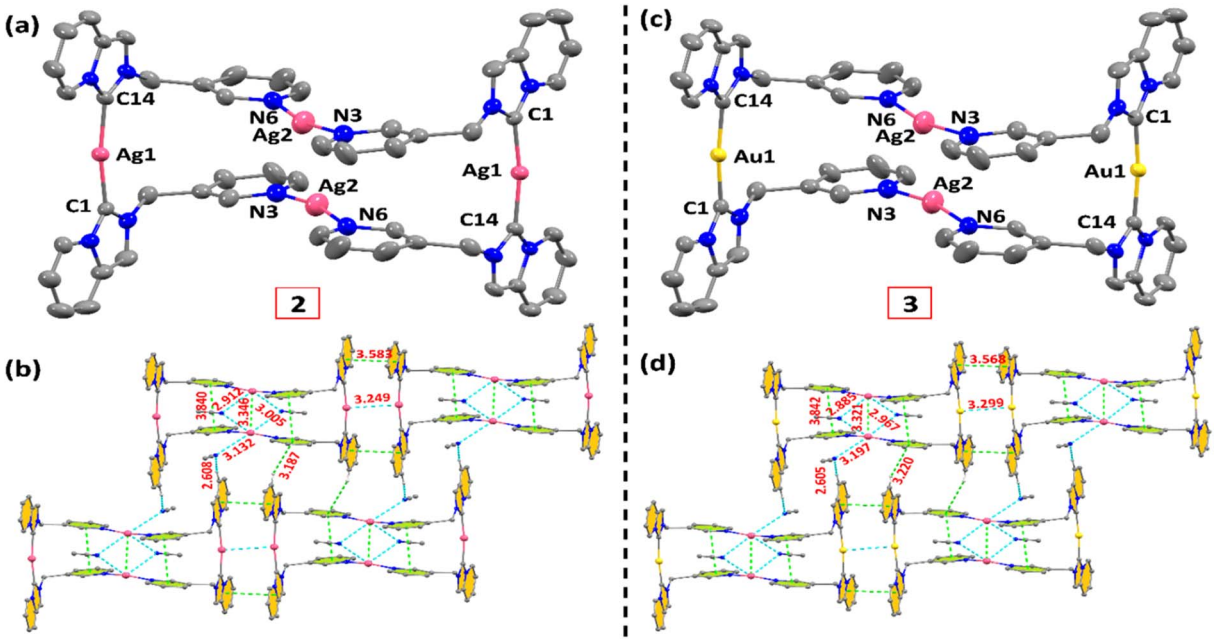

Fig. 1 Molecular structure of complexes **2**(a) and **3**(c) (hydrogen atoms, acetonitrile solvent and PF_6 are omitted for clarity). Selected bond lengths (Å) and angles (deg): for complex **2**: Ag(1)-C(1) 2.096(4), Ag(1)-C(14) 2.096(4), Ag(2)-N(3) 2.149(4), Ag(2)-N(6) 2.149(4), C(1)-Ag(1)-C(14) 171.11(14), N(3)-Ag(2)-N(6) 167.90(15); for complex **3**: Au(1)-C(1) 2.020(5), Au(1)-C(14) 2.021(4), Ag(2)-N(3) 2.146(5), Ag(2)-N(6) 2.137(4), N(6)-Ag(1)-N(3) 167.66(18), C(1)-Au(1)-C(14) 173.45(16). Packing diagram of complex **2**(b) Ag(2)-Ag(2) 3.2490(6) (intermolecular packing distance), Ag(2)-Ag(2) 3.3461(11) (intramolecular packing distance), and complex **3**(d), Ag(2)-Ag(2) 3.3205(13) (intramolecular packing distance), Au(1)-Au(1) 3.2991(4) (intermolecular packing distance).

is observed: one silver ion coordinates with two carbene carbon atoms from distinct ligands, while the other silver ion coordinates with pyridyl nitrogen atoms (N_{py}, where py = pyridine) from two different ligands. By contrast, the asymmetric unit of complex **3** consists of one Ag atom and one Au atom, where the softer carbene carbon center binds to Au(I) and the comparatively harder pyridyl nitrogen binds with Ag(I).

The Ag–$C_{carbene}$ bond lengths in complex **2** are 2.096(4) Å, while the Au–$C_{carbene}$ distances in complex **3** are slightly shorter, at 2.020(5) Å and 2.021(4) Å. The shorter Au–$C_{carbene}$ bond lengths compared to Ag–$C_{carbene}$ can indeed be attributed to relativistic effects. Ag–N_{py} bond distances range from 2.149(4) Å to 2.146(5) Å in both complexes (Table S2†). The $C_{carbene}$–Ag–$C_{carbene}$ bond angle in complex **2** is 171.11(14)°, showing a greater deviation from linearity compared to the $C_{carbene}$–Au–$C_{carbene}$ bond angle in complex **3**, which is 173.45(16)°. However, the N_{py}–Ag–N_{py} angles are very similar for both complexes, at 167.90(15)° for complex **2** and 167.66(18)° for complex **3** (Table S3†). These bond distances and angles align with reported values for Ag-carbene complexes.[28a] In both complexes **2** and **3**, two solvated CH_3CN molecules bridge two Ag(I) atoms that are bonded to the pyridyl nitrogen.[29] M–M weak interactions are found in complexes **2** and **3**: the intermolecular Ag(1)–Ag(1) separations (3.2490(6)Å) and intramolecular Ag(2)–Ag(2) separations (3.3461(11)Å) are observed in complex **2**, whereas intermolecular Au(1)–Au(1) interactions (3.2991(4)Å) and intramolecular Ag(1)–Ag(1) interactions (3.3205(13)Å) are observed in complex **3**. Various metal–metal, metal–solvent, and π···π stacking interactions contribute to the solid-state stability and promote the formation of 1D and 2D chain networks in both complexes, as illustrated in Fig. 1b and d. The powder X-ray diffraction (PXRD) patterns of complexes **2** and **3**, shown in Fig. S13,† are in good agreement with the simulated spectra, confirming the phase purity and isomorphism of complexes **2** and **3**.

Both molecules **2** and **3** possess several M–M interactions; these close-shell d^{10}–d^{10} interactions are expected to be a source of luminescence (as shown in Fig. 2).[30] Following excitation at 273 nm, the emission maxima for complexes **2** and **3** were observed at 382 and 379 nm, respectively. Time-resolved fluorescence analysis revealed that complexes **2** and **3** exhibit relatively long emission lifetimes. Notably, complex **2** demonstrated a higher average fluorescence lifetime of 3.56 ns, whereas it is 2.31 ns in the case of complex **3**, in DMSO at an excitation wavelength of 273 nm (as shown in Table S4†).[23] The lifetime of **1** HPF_6 could not be measured due to its low emission intensity.

The SEM images of complexes **2** and **3** reveal distinct differences in porosity (Fig. S14†). While both complexes exhibit a porous-like architecture, complex **2** demonstrates a significantly more porous structure compared to complex **3**. A more porous structure can have implications for conductivity-related applications.

The presence of coinage metals Ag and Au and the polymeric nature of complexes **2** and **3** prompted the study of their optoelectronic properties. Metal–semiconductor (MS) junction thin-film devices were used to collect the current–voltage (*I*–*V*) data under dark conditions and white light illumination. The Schottky behaviour of the MS junction devices is evidenced by the nonlinear rectifying nature of the graphs, as shown in Fig. 3.

The photoresponse was studied under AM1.5 radiation. All measurements were carried out at room temperature with a bias voltage range of ±1 V. The On/Off ratio of complex **3** was determined to be 3.3 in the dark and 10.9 under light, while for complex **2**, it improved to 3.5 in the dark and 21.5 under light, indicating the enhanced rectifying character of the silver-containing complex.

Under dark and light conditions, the conductivity of complex **2** was 4.6×10^{-9} S m^{-1} and 3.5×10^{-8} S m^{-1}, respectively, measured at room temperature, which decreased to 6.5×10^{-10} S m^{-1} and 3.3×10^{-9} S m^{-1} in complex **3** (shown in Table 1). The calculated value of photosensitivity for complex **2** was 6.98, which is 1.3 times greater than that of complex **3**, which showed a photosensitivity of 5.27. This substantial increase in photosensitivity indicates that the Ag complex **2** has greater light absorption properties than the Ag–Au mixed-metal complex **3**. All the estimated parameters (shown in Table 1) clearly indicate

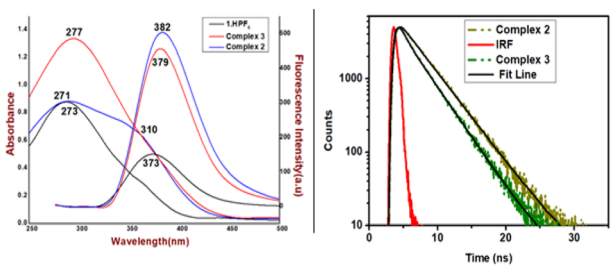

Fig. 2 (Left) absorption and emission spectra of **1** HPF_6, **2** and **3** recorded in CH_3CN at room temperature; (right) time-resolved fluorescence spectra of complexes **2** and **3**. The solid red line corresponds to the system's instrument response function (IRF).

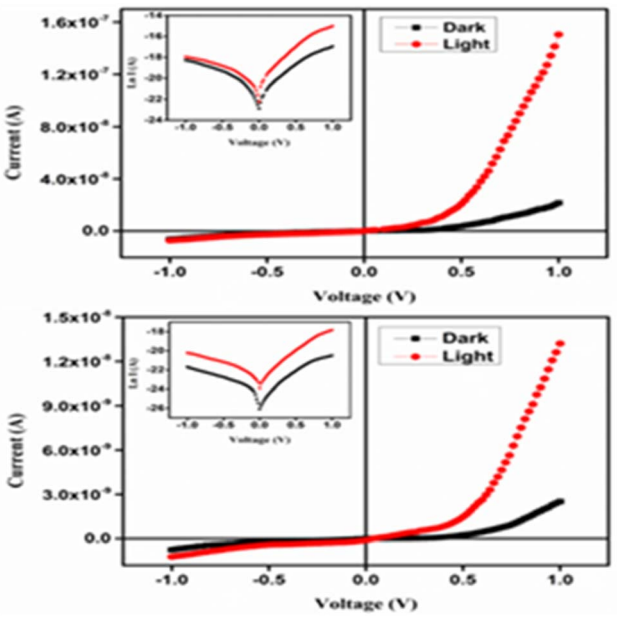

Fig. 3 Current–voltage (*I*–*V*) characteristics of complexes **2** (top) and **3** (bottom).

Table 1 Schottky diode parameters of complexes 2 and 3

Compd	Condition	On/off ratio	Conductivity (S m^{-1})	Ideality factor (n)	Barrier height (ϕ_B) eV	Series resistance, (R_S) Ω	
						dV/d ln I	$H(I)$
2	Dark	3.5	4.5×10^{-9}	1.46	0.75	3.43×10^{7}	8.26×10^{7}
	Light	21.5	3.5×10^{-8}	1.01	0.63	3.61×10^{6}	2.90×10^{7}
3	Dark	3.3	6.5×10^{-10}	0.88	1.05	2.67×10^{8}	3.76×10^{9}
	Light	10.9	3.3×10^{-9}	0.97	0.89	1.68×10^{7}	6.27×10^{7}

that complex **2**-based photovoltaic devices perform better compared to those based on complex **3**, and may be applied in a broad range of photovoltaic applications.[30] The shorter distances between tetranuclear units *via* M–M interactions and more compact π···π stacking interactions in complex **2**, compared to complex **3**, could be the reason for its superior performance as a photovoltaic device.

Cheung's equations were employed to study the various Schottky parameters such as ideality factor, series resistance, barrier height, *etc.*, and to compare the behaviour of devices based on complexes **2** and **3**. The value of the ideality factor (η) is very important, as it indicates the degree of ideal metal–semiconductor junction formation. The calculated values of η for both diodes under dark and illuminated conditions are listed in Table 1, where it was found that the formed MS junctions were not exactly ideal.

The deviation from ideal behaviour could be related to inhomogeneities in the Schottky barrier, along with the presence of interface states and series resistance at the junction.[28] The Schottky barrier height ($\varnothing_B$) is calculated using an alternative set of formulae, as illustrated below.

$$H(I) = V - \frac{nKT}{q}\ln\left(\frac{J}{AA^{*}T^{2}}\right) \quad (1)$$

$$H(I) = IR_S + n\varnothing_B \quad (2)$$

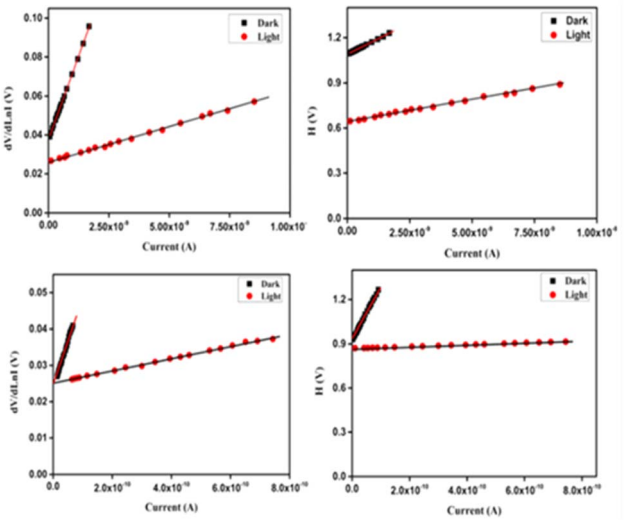

Fig. 4 dVd ln I and $H(v)$ graph of complexes **2** (top) and **3** (bottom).

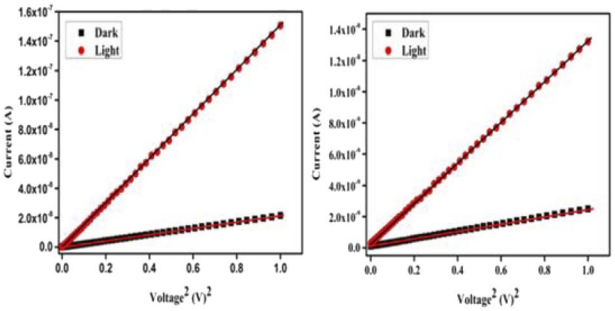

Fig. 5 Logarithm plot of I *vs.* V^2 for complexes **2** and **3**.

in this context, R_S represents the series resistance, while the other notations remain unchanged. The barrier potential is calculated from the intercept of the linear plot of $H(I)$ *vs.* current (Fig. 4). The series resistance value was also calculated from the slope of this graph and compared with previously determined values. To gain deeper insight into the charge transport mechanism, the I–V curves for both devices under dark and illuminated conditions were plotted on a logarithmic scale (Fig. 5). The plot reveals two distinct regions in the device, with Region-I exhibiting ohmic behavior, where the current is directly proportional to voltage due to thermionic emission. The I–V curve suggests that tunneling is the major contributing factor.[31] Region-II follows a power-law behavior, where the charge transport mechanism aligns with the space-charge-limited current (SCLC) theory. Based on the SCLC model, the effective carrier mobility (μ_{eff}) is estimated from the higher voltage region of the I *vs.* V^2 plot (Fig. 5) using the Mott–Gurney equation.

The dielectric constant (ε_r) was determined by plotting the capacitance *vs.* frequency graph (Fig. 6). Using the capacitance

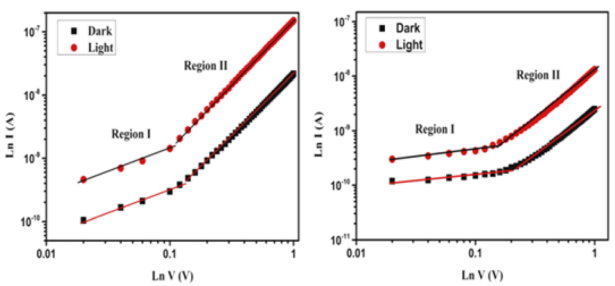

Fig. 6 Capacitance *vs.* frequency for **2** and **3**.

Table 2 Charge transport parameters of complexes **2** and **3**

Compd	Condition	Mobility, μ_{eff} ($cm^2\ V^{-1}\ s^{-1}$)	Carrier concentration N (m^{-3})	Lifetime (τ) (sec)	Diffusion coefficient D ($m^2\ s^{-1}$)	Diffusion length L_D (m)
2	Dark	3.39×10^{-23}	8.43×10^{32}	3.06×10^{15}	8.77×10^{-25}	7.33×10^{-5}
	Light	2.37×10^{-22}	9.31×10^{32}	3.23×10^{14}	6.13×10^{-24}	6.29×10^{-5}
3	Dark	2.67×10^{-24}	1.52×10^{33}	3.48×10^{16}	6.90×10^{-26}	6.93×10^{-5}
	Light	1.44×10^{-23}	1.45×10^{33}	8.13×10^{15}	3.72×10^{-25}	7.78×10^{-5}

value at the saturation level, ε_r was calculated with the following equation.[3]

$$\varepsilon_r = \frac{CL}{\varepsilon_0 A} \quad (3)$$

The diode parameters of complex **2** exhibit significantly improved charge-transfer kinetics after light soaking, compared to **3** (Table 2). Such materials hold great potential for advancing photosensitive device applications in the future.

Experimental section

2-Pyridine carboxaldehyde, 3-picolylamine, and Ag_2O were supplied by Sigma-Aldrich, UK. All reagents used in synthesis and analysis were of analytical grade and utilized without additional purification. Solvents were dried (when necessary) following established protocols, and all experimental procedures were conducted under open air conditions. ^{1}H NMR and ^{13}C NMR spectra were recorded using a Bruker spectrometer at 400 and 100 MHz, respectively. For ^{1}H and ^{13}C NMR, chemical shifts (δ) are reported in ppm relative to the internal standard TMS, with coupling constants (J) given in Hz. Elemental analysis was carried out using a PerkinElmer 2400C elemental analyzer. A Cary 100 Bio spectrophotometer (Agilent Technologies) was used to record UV-visible spectra ranging from 200 to 800 nm. Emission spectra were obtained using a Cary Eclipse fluorescence spectrophotometer (Agilent Technologies). Time-resolved fluorescence measurements were conducted with a LifeSpec II TCSPC spectrometer, utilizing a 330 nm picosecond diode laser (EPL) as the excitation source. The FTIR spectra of the compounds were recorded using a PerkinElmer 2000 system spectrometer. Electrospray ionization mass spectra were recorded using an Agilent 6538 Ultra-High Definition (UHD) Accurate Mass Q-TOF spectrometer. The photoresponse was studied using AM1.5 radiation. All the measurements were carried out at room temperature at bias voltage range of ± 1 V.

Crystal structure determination

Using Bruker Smart Apex-II CCD diffractometer the Single-crystal X-ray diffraction data were collect at 273 K using Mo Kα radiation ($\lambda = 0.71073$ Å). The intensity data were processed and integrated using Bruker SAINT-plus software, with absorption corrections were made using the SADABS program.[32] The structures were determined using direct methods in SHELXT 2014/5 and refined through full-matrix least squares techniques on F^2 with SHELXL 2018/3,[33] integrated within the OleX2 software.[34] Disorder within the molecule was also modeled using OleX2. Anisotropic thermal displacement parameters were applied for non-hydrogen atoms, while hydrogen atoms were positioned in idealized geometries and refined using a riding model, with isotropic thermal parameters set at 1.2 or 1.5 times those of their parent atoms. Crystal structures and packing diagrams for the isomeric complexes were visualized and generated using Mercury 4.3.1 and POV-Ray software. Key crystallographic parameters, along with details of the structure determination and refinement, are summarized in Table S1.†

Synthesis of 3-(pyridylmethyl)imidazo[1,5-*a*]pyridin-4-ylium hexafluorophosphate, (1 HPF_6)

Pyridine 2-carboxaldehyde (1500 mg, 14 mmol) and 3-picolylamine (1500 mg, 14 mmol) were dissolved in toluene and stirred for 10 h. Then, the mixture of Schiff base (*E*)-1-(pyridin-2-yl)-*N*-(pyridin-3-ylmethylene)methanamine (2400 mg, 12 mmol) and crushed 91% paraformaldehyde powder (75.6 mg, 2.70 mmol) were stirred for 8 h. 5 ml of 4(N) HCl in Et_2O were added slowly, resulting in immediate layer separation. Lower viscous yellowish layer was separated and aqueous KPF_6 was added to the solution, leading to the immediate formation of a white precipitate. The precipitate was filtered and recrystallized from acetonitrile and diethyl ether. The solid product was dried. Yield was 2650 mg (7.46 mmol, 86.66%). ^{1}H NMR (400 MHz, DMSO-d6), δ (ppm): 9.77 (s, 1H, H^k), 8.84 (s, 1H, H^e), 8.72 (d, J = 4.9 Hz, 1H, H^a), 8.56 (d, J = 7.1 Hz, 1H, H^h), 8.23 (s, 1H, H^i), 8.17 (d, J = 7.9 Hz, 1H, H^f), 7.79 (d, J = 9.3 Hz, 1H, H^d), 7.68 (dd, J = 7.9, 5.2 Hz, 1H, H^c), 7.22 (dd, J = 17.3, 8.1 Hz, 1H, H^b), 7.14 (t, J = 6.9 Hz, 1H, H^g), 5.82 (s, 1H, H^j). ^{13}C NMR (100 MHz, DMSO-d6), δ (ppm): 147.71, 140.69, 132.38, 130.23, 127.43, 125.73, 125.40, 124.96, 118.72, 118.23, 118.05, 113.80, 50.75. Anal. calc. for $C_{13}H_{12}N_3PF_6$: C, 43.94; H, 3.38; N, 11.83; found: C, 43.71; H, 3.34; N, 11.76%. HRMS (ESI): $C_{13}H_{12}N_3$ [1 H]$^+$ = 210.1031 m/z (calcd) found: 210.1021 m/z.

Synthesis of $[Ag_4(1)_4][PF_6]_4 \cdot 4MeCN$

Proligand **1** HPF_6 (200 mg, 0.56 mmol) and Ag_2O (130.5 mg, 0.56 mmol) were mixed in acetonitrile. The mixture was stirred at room temperature in the dark until most of the Ag_2O disappeared. The solution was filtered through a plug of Celite to remove the excess of Ag_2O. The clear filtrate was then evaporated to dryness to get crude complex **2** as solid. Slow diffusion

of diethyl ether into CH_3CN solution of crude complex **2** yielded a crystalline material. Yield was 257.8 mg, (0.13 mmol, 78%).^{1}H NMR (400 MHz, DMSO-d6), δ (ppm): 8.84 (s, 1H, H^e), 8.78 (d, J = 4.5 Hz, 1H, H^a), 8.66 (d, J = 7.2 Hz, 1H, H^d), 8.42 (s, 1H, H^i), 8.24 (d, J = 4.7 Hz, 1H, H^f), 8.20 (d, J = 6.3 Hz, 1H, H^h), 7.71 (m, J = 7.65 Hz, 1H,H^g), 7.38 (t, J = 9.1, Hz, 1H, H^b), 7.31 (t, J = 9.1 Hz, 1H, H^c), 5.82 (s, 2H, H^j). ^{13}C NMR (100 MHz, DMSO-d6), δ (ppm): 165.02, 148.75, 148.34, 135.3 3, 128.05, 125.85, 125.60, 124.90, 122.60, 119.11, 118.32, 114.26, 50.92. Anal. calc. for $C_{60}H_{56}N_{16}Ag_4P_4F_{24}$: C, 35.81; H, 2.80; N, 11.13; found: C, 35.18; H, 2.36; N, 10.65%. ESI-MS: *m/z* observed at 1175.1194 for $[Ag_3(\mathbf{1})_2]3PF_6$.

Synthesis of $[Ag_2–Au_2(\mathbf{1})_4][PF_6]_4\cdot 4MeCN$

At room temperature, complex **2** (300 mg, 0.16 mmol) was dissolved in 10 ml of acetonitrile. The acetonitrile solution (5 ml) of $Au(SMe_2)Cl$ (24 mg, 0.08 mmol) was added dropwise to the complex **2** solution. After 2 h of stirring, the solution changed to light yellow colour and a white precipitate of AgCl appeared. After filtration, the resulting solution was evaporated and a light yellow powder was collected. The crude product was recrystallized by slow diffusion of diethyl ether into acetonitrile solution of **3**. Yield was 256 mg (0.013 mmol, 79%). ^{1}H NMR (400 MHz, DMSO-d6), δ (ppm): 8.87 (s, 1H, H^e), 8.84 (d, J = 4.5 Hz, 1H, H^a), 8.72 (d, J = 7.2 Hz, 1H, H^d), 8.61 (s, 1H, H^i), 8.47 (d, J = 4.8 Hz, 1H, H^f), 8.27 (d, J = 6.3 Hz, 1H, H^h), 7.78 (m, 1H, H^g),7.52 (t, J = 9.1 Hz, 2H, H^b), 7.35 (t, J = 9.3 Hz, 1H, H^c), 5.82 (s, 2H, H^j).^{13}C NMR (100 MHz, DMSO-d6), δ (ppm): 173.02, 148.65, 147.60, 135.20, 128.04, 125.71, 125.68, 125.60, 122.82, 118.33, 118.10, 114.63,50.98. Anal. calc. for $C_{60}H_{56}N_{16}Ag_2Au_2P_4F_{24}$: C, 32.89; H, 2.58; N, 10.23; found: C, 32.32; H, 2.06; N, 9.75%. ESI-MS: *m/z* observed at 615.1282 for $[Au(\mathbf{1})_2]^+$ and 867.0345 for $[[AuAg(\mathbf{1})_2]PF_6]^+$.

Conclusion

In summary, in this manuscript we have described the synthesis, characterization and application of tetranuclear coinage metal-hybrid NHC complexes. The work also reports a heterobimetallic Ag_2Au_2 complex, synthesized *via* a selective transmetallation pathway from the tetranuclear silver-NHC congener. The compounds have furthermore been tested for photoelectric applications to create devices with novel capabilities, and it was observed that complex **2** is more efficient than the complex **3**. The shorter distances between tetranuclear units *via* M–M interactions and more compact $\pi\cdots\pi$ stacking interactions in complex **2**, compared to complex **3**, could be the reason for its better performance as a photovoltaic device. Further modification of the ligand framework might lead to more impactful photoconductive properties.

Data availability

The supplemental crystallographic data for this paper are contained in CCDC 2271882 (for **2**), and CCDC 2271883 (for **3**). These data can be obtained free of charge from the Cambridge Crystallographic Data Centre *via* **www.ccdc.cam.ac.uk/data_request/cif**.

Author contributions

The manuscript was written through contributions of all authors. All authors have given approval to the final version of the manuscript.

Conflicts of interest

There are no conflicts of interest to declare.

Acknowledgements

JD is grateful to Utkal University and RUSA 2. O for funding.

References

1 (*a*) R. Chakrabarty, P. S. Mukherjee and P. J. Stang, *Chem. Rev.*, 2011, **111**, 6810–6918; (*b*) A. Goswami, S. Saha, P. K. Biswas and M. Schmittel, *Chem. Rev.*, 2020, **120**, 125–199; (*c*) M. Fujita, M. Tominaga, A. Hori and B. Therrien, *Acc. Chem. Res.*, 2005, **38**, 369–378; (*d*) W.-X. Gao, H.-J. Feng, B.-B. Guo, Y. Lu and G.-X. Jin, *Chem. Rev.*, 2020, **120**, 6288–6325; (*e*) M. Yoshizawa and L. Catti, *Acc. Chem. Res.*, 2019, **52**, 2392–2404; (*f*) D. Fujita, Y. Ueda, S. Sato, N. Mizuno, T. Kumasaka and M. Fujita, *Nature*, 2016, **540**, 563–566; (*g*) S. Hiraoka, K. Harano, M. Shiro, Y. Ozawa, N. Yasuda, K. Toriumi and M. Shionoya, *Angew. Chem., Int. Ed.*, 2006, **45**, 6488–6491; (*h*) S.-C. Wang, K.-Y. Cheng, J.-H. Fu, Y.-C. Cheng and Y.-T. Chan, *J. Am. Chem. Soc.*, 2020, **142**, 16661–16667; (*i*) L.-X. Cai, D.-N. Yan, P.-M. Cheng, J.-J. Xuan, S.-C. Li, L.-P. Zhou, C.-B. Tian and Q.-F. Sun, *J. Am. Chem. Soc.*, 2021, **143**, 2016–2024.

2 (*a*) J. Meeuwissen and J. N. Reek, *Nat. Chem.*, 2010, **2**, 615–621; (*b*) S. De, K. Mahata and M. Schmittel, *Chem. Soc. Rev.*, 2010, **39**, 1555–1575; (*c*) J.-R. Li and H.-C. Zhou, *Nat. Chem.*, 2010, **2**, 893–898; (*d*) M. Yamanaka, Y. Yamada, Y. Sei, K. Yamaguchi and K. Kobayashi, *J. Am. Chem. Soc.*, 2006, **128**, 1531–1539; (*e*) Q.-F. Sun, S. Sato and M. Fujita, *Angew. Chem., Int. Ed.*, 2014, **53**, 13510–13513; (*f*) J.-F. Ayme, J. E. Beves, C. J. Campbell and D. A. Leigh, *J. Am. Chem. Soc.*, 2019, **141**, 3605–3612; (*g*) G. Li, Z. Zhou, C. Yuan, Z. Guo, Y. Liu, D. Zhao, K. Liu, J. Zhao, H. Tan and X. Yan, *Angew. Chem., Int. Ed.*, 2020, **59**, 10013–10017.

3 (*a*) P. Mal, B. Breiner, K. Rissanen and J. R. Nitschke, *Science*, 2009, **324**, 1697–1699; (*b*) F. J. Rizzuto, L. K. S. von Krbek and J. R. Nitschke, *Nat. Chem. Rev.*, 2019, **3**, 204–222; (*c*) K. Niki, T. Tsutsui, M. Yamashina, M. Akita and M. Yoshizawa, *Angew. Chem., Int. Ed.*, 2020, **59**, 10489–10492; (*d*) P. Howlader, B. Mondal, P. C. Purba, E. Zangrando and P. S. Mukherjee, *J. Am. Chem. Soc.*, 2018, **140**, 7952–7960; (*e*) L.-J. Wang, X. Li, S. Bai, Y.-Y. Wang and Y.-F. Han, *J. Am. Chem. Soc.*, 2020, **142**, 2524–2531; (*f*) L. Xu, D. Zhang, T. K. Ronson and J. R. Nitschke, *Angew. Chem., Int. Ed.*, 2020, **59**, 7435–7438; (*g*) M. Kieffer, R. A. Bilbeisi,

J. D. Thoburn, J. K. Clegg and J. R. Nitschke, *Angew. Chem., Int. Ed.*, 2020, **59**, 11369–11373.

4 (*a*) M. Zhang, M. L. Saha, M. Wang, Z. Zhou, B. Song, C. Lu, X. Yan, X. Li, F. Huang, S. Yin and P. J. Stang, *J. Am. Chem. Soc.*, 2017, **139**, 5067–5074; (*b*) A. J. McConnell, C. S. Wood, P. P. Neelakandan and J. R. Nitschke, *Chem. Rev.*, 2015, **115**, 7729–7793; (*c*) M. L. Saha, X. Yan and P. J. Stang, *Acc. Chem. Res.*, 2016, **49**, 2527–2539; (*d*) X. Yan, H. Wang, C. E. Hauke, T. R. Cook, M. Wang, M. L. Saha, Z. Zhou, M. Zhang, X. Li, F. Huang and P. J. Stang, *J. Am. Chem. Soc.*, 2015, **137**, 15276–15286.

5 (*a*) M. Yoshizawa, M. Tamura and M. Fujita, *Science*, 2006, **312**, 251–254; (*b*) D. M. Kaphan, M. D. Levin, R. G. Bergman, K. N. Raymond and F. D. Toste, *Science*, 2015, **350**, 1235–1238; (*c*) C. J. Brown, F. D. Toste, R. G. Bergman and K. N. Raymond, *Chem. Rev.*, 2015, **115**, 3012–3035; (*d*) L. J. Jongkind, X. Caumes, A. P. T. Hartendorp and J. N. H. Reek, *Acc. Chem. Res.*, 2018, **51**, 2115–2128; (*e*) Y. Fang, J. A. Powell, E. Li, Q. Wang, Z. Perry, A. Kirchon, X. Yang, Z. Xiao, C. Zhu, L. Zhang, F. Huang and H.-C. Zhou, *Chem. Soc. Rev.*, 2019, **48**, 4707–4730; (*f*) V. Martí-Centelles, A. L. Lawrence and P. J. Lusby, *J. Am. Chem. Soc.*, 2018, **140**, 2862–2868; (*g*) Q.-Q. Wang, S. Gonell, S. H. A. M. Leenders, M. Dürr, I. IvanovićBurmazović and J. N. H. Reek, *Nat. Chem.*, 2016, **8**, 225–230; (*h*) J. Guo, Y.-Z. Fan, Y.-L. Lu, S.-P. Zheng and C.-Y. Su, *Angew. Chem., Int. Ed.*, 2020, **59**, 8661–8669; (*i*) C. Tan, J. Jiao, Z. Li, Y. Liu, X. Han and Y. Cui, *Angew. Chem., Int. Ed.*, 2018, **57**, 2085–2090.

6 (*a*) T. R. Cook and P. J. Stang, *Chem. Rev.*, 2015, **115**, 7001–7045; (*b*) A. M. Castilla, W. J. Ramsay and J. R. Nitschke, *Acc. Chem. Res.*, 2014, **47**, 2063–2073.

7 M. Poyatos, J. A. Mata and E. Peris, *Chem. Rev.*, 2009, **109**, 3677–3707.

8 (*a*) M. Fujita, *Chem. Soc. Rev.*, 1998, **27**, 417–425; (*b*) A. J. McConnell, C. S. Wood, P. P. Neelakandan and J. R. Nitschke, *Chem. Rev.*, 2015, **115**, 7729–7793; (*c*) A. Rit, T. Pape and F. E. Hahn, *J. Am. Chem. Soc.*, 2010, **132**, 4572–4573; (*d*) M.-M. Gan, J.-Q. Liu, L. Zhang, Y.-Y. Wang, F. E. Hahn and Y.-F. Han, *Chem. Rev.*, 2018, **118**, 9587–9641.

9 A. J. Boydston and C. W. Bielawski, *Dalton Trans.*, 2006, **34**, 4073–4077.

10 A. Pöthig and A. Casini, *Theranostics*, 2019, **9**, 3150–3169.

11 (*a*) J. Kim, D. Nam, H. Kitagawa, D.-W. Lim and W. Choe, *Nano Res.*, 2021, **14**, 392–397; (*b*) F. M. Conrady, R. Fröhlich, C. Schulte to Brinke, T. Pape and F. E. Hahn, *J. Am. Chem. Soc.*, 2011, **133**, 11496–11499; (*c*) M. Schmidtendorf, T. Pape and F. E. Hahn, *Angew. Chem., Int. Ed.*, 2012, **51**, 2195–2198; (*d*) C. Mejuto, G. Guisado-Barrios, D. Gusev and E. Peris, *Chem. Commun.*, 2015, **51**, 13914–13917.

12 (*a*) D. H. Wang, B. G. Zhang, C. He, P. Y. Wu and C. Y. Duan, *Chem. Commun.*, 2010, **46**, 4728–4730; (*b*) C. Segarra, G. Guisado-Barrios, F. E. Hahn and E. Peris, *Organometallics*, 2014, **33**, 5077–5080; (*c*) N. Sinha, F. Roelfes, A. Hepp, C. Mejuto, E. Peris and F. E. Hahn, *Organometallics*, 2014, **33**, 6898–6904; (*d*) N. Sinha, L. Stegemann, T. T. Y. Tan, N. L. Doltsinis, C. A. Strassert and F. E. Hahn, *Angew. Chem., Int. Ed.*, 2017, **56**, 2785–2789; (*e*) Y. Li, Y. Y. An, J. Z. Fan, X. X. Liu, X. Li, F. E. Hahn, Y. Y. Wang and Y. F. Han, *Angew. Chem., Int. Ed.*, 2020, **59**, 10073–10080; (*f*) Y. Li, M.-Z. Han, X.-T. Chang, L. Zhang, L.-L. Ma, L.-Y. Sun, F. E. Hahn and Y.-F. Han, *CCS Chem.*, 2024, 1–11.

13 C. Radloff, J. J. Weigand and F. E. Hahn, *Dalton Trans.*, 2009, **43**, 9392–9394.

14 M. Schmidtendorf, C. Schulte to Brinke and F. E. Hahn, *J. Organomet. Chem.*, 2014, **751**, 620–627.

15 M. Schmidtendorf, T. Pape and F. E. Hahn, *Dalton Trans.*, 2013, **42**, 16128–16141.

16 A. Sinha, F. Roelfes, A. Hepp and E. F. Hahn, *Chem.–Eur. J.*, 2017, **23**, 5939–5942.

17 (*a*) F. E. Hahn, C. Radloff, T. Pape and A. Hepp, *Organometallics*, 2008, **27**, 6408–6410; (*b*) C. Radloff, F. E. Hahn, T. Pape and R. Fröhlich, *Dalton Trans.*, 2009, **35**, 7215–7222.

18 (*a*) P. C. Purba, M. Venkateswaralu, S. Bhattacharyya and P. S. Mukherjee, *Inorg. Chem.*, 2022, **61**, 713–722; (*b*) P. K. Maitra, S. Bhattacharyya, P. C. Purba and P. S. Mukherjee, *Inorg. Chem.*, 2024, **63**, 2569–2576; (*c*) P. C. Purba, P. K. Maitra, S. Bhattacharyya and P. S. Mukherjee, *Inorg. Chem.*, 2023, **62**, 11037–11043.

19 (*a*) P. J. Altmann and A. Pöthig, *J. Am. Chem. Soc.*, 2016, **138**, 13171–13174; (*b*) P. J. Altmann and A. Pöthig, *Angew. Chem., Int. Ed.*, 2017, **56**, 15733–15736.

20 R. C. Nishad, S. Kumar and A. Rit, *Angew. Chem., Int. Ed.*, 2022, **61**, e202206788.

21 S. Ibańez, M. Poyatos and E. Peris, *Acc. Chem. Res.*, 2020, **53**, 1401–1413.

22 B. K. Rana, V. Bertolasi, S. Pal, P. Mitra and J. Dinda, *J. Mol. Strur.*, 2013, **1049**, 458–463.

23 P. Sahu, N. C. Jana, S. Barik, H. K. Kisan, A. Changotra, A. A. Isab and J. Dinda, *Dalton Trans.*, 2024, **53**, 1099–1104.

24 D. M. Roundhill and . P. Fackler, *Optoelectronic Properties of Inorganic Compounds*, Springer, USA, 2013.

25 (*a*) S. Bente, F. Kampert, T. T. Y. Tan and F. E. Hahn, *Chem. Commun.*, 2018, **54**, 12887; (*b*) P. D. Dutschke, S. Bente, C. G. Daniliuc, J. Kinas, A. Hepp and F. E. Hahn, *Dalton Trans.*, 2020, **49**, 14388–14392.

26 (*a*) C. Cesari, B. Berti, F. Calcagno, C. Lucarelli, M. Garavelli, R. Mazzoni, I. Rivalta and S. Zacchini, *Organometallics*, 2021, **40**, 2724–2735; (*b*) M. Redrado, A. Benedi, I. Marzo, A. L. G. -Otín, V. F. -Moreira and M. C. Gimeno, *Chem.–Eur. J.*, 2021, **27**, 9885–9897; (*c*) G. Mo, Q. Wang, W. Lu, C. Wang and P. Li, *Chin. J. Chem.*, 2023, **41**, 335–354.

27 (*a*) L. S. Xie, E. V. Alexandrov, G. Skorupskii, D. M. Proserpio and M. Dincă, *Chem. Sci.*, 2019, **10**, 8558–8565; (*b*) E. M. Johnson, S. Iiic and A. J. Morris, *ACS Cent. Sci.*, 2021, **7**, 445–453; (*c*) Y. W. Zhang, Y. Lu, L. Y. Sun, P. D. Dutschke, M. M. Gan, L. Zhang, A. Hepp, Y. F. Han and F. E. Hahn, *Angew. Chem.*, 2023, **135**, e202312323.

28 (*a*) J. Dinda, T. Samanta, A. Nandy, K. D. Saha, S. K. Seth, S. K. Chattopadhyay and C. W. Bielawski, *New J. Chem.*, 2014, **38**, 1218–1224; (*b*) B. K. Rana, A. Nandy, V. Bertolasi,

C. W. Bielawski, K. D. Saha and J. Dinda, *Organometallics*, 2014, **33**, 2544–2548.

29 (*a*) V. J. Catalano and A. L. Moore, *Inorg. Chem.*, 2005, **44**, 6558–6566; (*b*) V. J. Catalano and M. A. Malwitz, *Inorg. Chem.*, 2003, **42**, 5483–5485.

30 M. Das, J. Datta, A. Dey, R. Jana, A. Layek, S. Middya and P. P. Ray, *RSC Adv.*, 2015, **5**, 101582.

31 A. Dey, S. Middya, R. Jana, M. Das, J. Datta, A. Layek and P. P. Ray, *J. Mater. Sci.: Mater. Electron.*, 2016, **27**, 6325–6335.

32 G. M. Sheldrick, *SADABS*, University of Göttingen, Germany, 1996.

33 G. M. Sheldrick, *ActaCrystallogr., Sect. A: Found. Crystallogr.*, 2008, **64**, 112.

34 O. V. Dolomanov, L. J. Bourhis, R. J. Gildea, J. A. K. Howard and H. Puschmann, *J. Appl. Cryst.*, 2009, **42**, 339–341.